Catalysis Science & Technology

ROYAL SOCIETY OF CHEMISTRY

PAPER

View Article Online
View Journal | View Issue

Cite this: *Catal. Sci. Technol.*, 2024, 14, 3984

Penta- *versus* hexa-coordinated iridium catalysts control the reactivity of the direct reductive amination between aliphatic amines and aliphatic ketones: a DFT-guided mechanism†

Hao Lin,[a] Longfei Li, *[a] Lanbo Liu,[a] Zhihui Li,[a] Thi-Mo Nguyen,[b] Matthieu Jouffroy[c] and Rafael Gramage-Doria *[b]

Received 22nd April 2024,
Accepted 13th June 2024

DOI: 10.1039/d4cy00516c

rsc.li/catalysis

Understanding reaction mechanisms of metal-catalyzed processes is of paramount importance for the design of superior catalysts that circumvent unproductive pathways, while accelerating catalyst discovery. In this respect, gaining mechanistic understanding for reactions carried out at high pressures of gas reagents remains a major limitation because special setups are typically required, which is the case for metal-catalyzed direct reductive aminations (DRA) under high H_2 pressure. To overcome this issue, extensive computational calculations have been herein conducted for the iridium-catalyzed DRA between aliphatic ketones and aliphatic secondary amines. This highly atom-economic reaction delivers only water as side-product and it is relevant for the identification of active pharmaceutical ingredients. In this contribution, we highlight that the excellent reactivity encountered with very different P,P-chelating ligands results from the fact that two different mechanistic pathways operate for each system. In addition, we found that the key hydride transfer step is more accessible with a penta-coordinated iridium complex rather than with the expected hexa-coordinated iridium species using a Josiphos-type ligand when compared to the large bite-angle Xantphos. For comparison purposes, we also evaluated a related Josiphos-type ligand and a small bite-angle diphosphane.

Introduction

The fine-understanding of the exact mode of action of metal catalysts is of high relevance for the development of more powerful systems.[1–3] In this regard, in-depth kinetic studies utilizing *in situ* or operando spectroscopy techniques are very useful to identify reaction intermediates while postulating reaction pathways.[4–6] However, homogeneous catalytic reactions involving the use of gas reagents imply very demanding set-ups to monitor these processes, thus significantly limiting the gain of mechanistic insights.[7–15] On the other hand, computational calculations by means of state-of-the-art density functional theory (DFT) protocols enable the identification of reaction pathways for explaining the selectivity and/or the activity reached with a given metal catalyst.[16–23] This is particularly advantageous for homogeneous metal-catalysed reactions involving gaseous reagents such as H_2, CO, CO_2, and others, which are routinely employed in hydrogenations, hydroformylations, (alkoxy) carbonylations, carboxylations and related ones, including also the asymmetric variants.[24–39]

In this context, H_2-mediated direct reductive aminations (DRA) catalysed by metal complexes derived mainly from Rh, Ru, Ir, Pd, Fe and Co, are very attractive as they enable the formal coupling of a ketone (or aldehyde) with a primary or secondary amine leading to the corresponding secondary or tertiary amine (Fig. 1A and B).[40–44] This type of reaction meets several green chemistry principles since it is highly atom economical, benign water is formed as side-product and low catalyst loading is typically used, thus resulting in a significantly low environmental impact[45–51] when compared to the use of over-stoichiometric amounts of hazardous reducing agents such as lithium, aluminium or boron hydrides, or organosilanes.[52–57] Of particular importance is the access to tertiary amines *via* H_2-mediated DRA because they are ubiquitous in materials and pharmaceutical

[a] College of Pharmacy, Key Laboratory of Pharmaceutical Quality Control of Hebei Province, Key Laboratory of Medicinal Chemistry and Molecular Diagnosis of Ministry of Education, Hebei University, Baoding 071002, Hebei, P. R. China. E-mail: lilongfei@hbu.edu.cn
[b] Univ. Rennes, CNRS, ISCR–UMR6226, F-35000 Rennes, France. E-mail: rafael.gramage-doria@univ-rennes1.fr
[c] Chemical Process R&D, Discovery Process Research, Janssen Pharmaceutica N.V, Turnhoutseweg 30, 2340 Beerse, Belgium

† Electronic supplementary information (ESI) available: *xyz* cartesian coordinates. See DOI: https://doi.org/10.1039/d4cy00516c

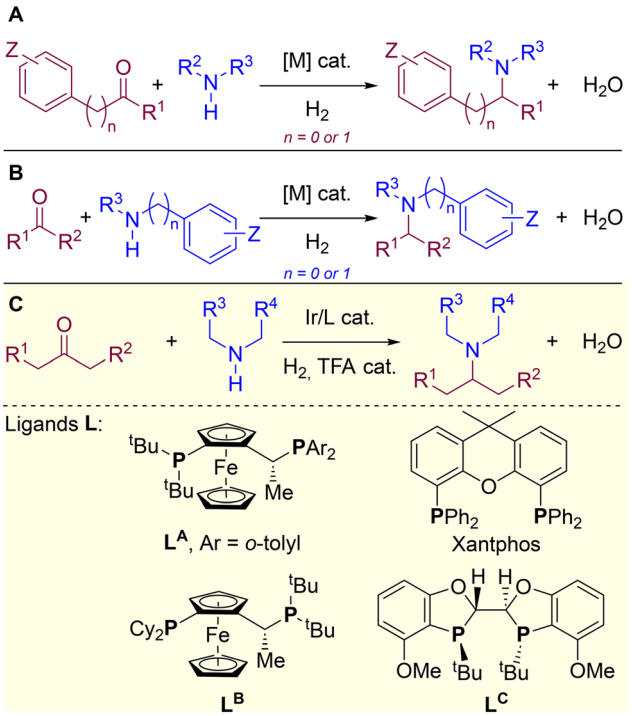

Fig. 1 Transition metal-catalysed DRA reactions: (A and B) state-of-the-art with biased substrates and (C) prior work with unbiased substrates highlighting the structure of relevant P,P-chelating diphosphane ligands, whose mechanism is herein studied by DFT calculations. R = H, alkyl or aryl.

sciences.[58–64] However, the substrate scope of metal-catalysed DRA is limited to pre-activated amines and carbonyl-containing partners directly connected to an aromatic or benzylic fragment (Fig. 1A and B).[65–82] In order to span H_2-mediated DRA towards purely aliphatic systems, we have pioneered the very first report on the identification of an iridium/diphosphane system that overcomes this limitation, thereby enabling to successfully utilize completely unbiased aliphatic ketones and aliphatic amines (Fig. 1C).[83] During this initial investigation, an important task was devoted to the identification of the most suitable ligand leading, unexpectedly, to ligands with a very different backbone structures, namely Josiphos-type ligand **L**$^{\mathbf{A}}$ and Xantphos (Fig. 1C).[83] Due to the difficulty to identify and characterize active iridium species under catalytically-relevant conditions (50 bar of H_2), we turned our attention to study the whole catalytic cycle of the reaction by means of computational calculations. Herein, we present an in-depth DFT study that shows that the H_2-mediated DRA between aliphatic ketones and aliphatic amines with iridium catalysis undergoes a completely different pathway depending on the nature of the ligand, being possible to reach high reactivity in both scenarios. We also found that two other ligands, commonly used for hydrogenation processes (Josiphos-type **L**$^{\mathbf{B}}$ and BIBOP-type **L**$^{\mathbf{C}}$), are not appropriate for this iridium-catalysed DRA, as they promote competitive side-reactions. In addition, the role of the trifluoroacetate anion was analysed and it was found that, depending on the coordinating ability, it can lead to the stabilization of iridium species of different coordination geometry, which dramatically influence one of the key steps of the catalytic cycle, namely the hydride transfer step from the metal to the substrate. Other metal-based catalytic systems have been recently reported for the formation of purely aliphatic (chiral) amines.[84–87]

Results and discussion

Initial considerations

In a previous contribution, we disclosed the iridium-catalysed DRA between aliphatic ketones and aliphatic amines leading selectively to tertiary aliphatic amines under 50 bar of H_2 (Scheme 1).[83] After extensive screening, the optimal reaction conditions identified comprised the use of 2 mol% of $[Ir(COD)Cl]_2$ (COD = 1,5-cyclooctadiene) dimer as the pre-catalyst and 4 mol% of a P,P-chelating ligand in the presence of 30 mol% of trifluoroacetic acid (TFA) in methanol solution at room temperature. Under these precise reaction conditions, the catalysis with the Josiphos-type ligand **L**$^{\mathbf{A}}$ and Xantphos led, surprisingly, to equally efficient results with almost full conversion and exclusive formation of the product **3** starting from ketone **1** and the secondary amine **2**. The difference in isolated yields was ascribed to the difficult, non-trivial purification of **3** during the column chromatography process. As such, for the DFT study of the reaction mechanism, we focused in the reaction involving ketone **1** and amine **2** partners, and compared the reaction coordinate trajectory by varying the nature of the ligand. Because little enantioselective induction (<20% ee) was found using pro-chiral ketones such as 2-butanone, in this study we focused on a relatively simple substrate model involving cyclohexanone (**1**) that leads to an achiral product **3**.

In accordance with previous theoretical studies, we adopted the DFT ωB97X-D method[88] in this study using the Gaussian 09 program.[89] The geometric structures in methanol solution were optimized using BS-I basis sets, in which 6-311G(d,p) basis sets were used for non-metallic atoms, and SDD basis sets with effective core potential were

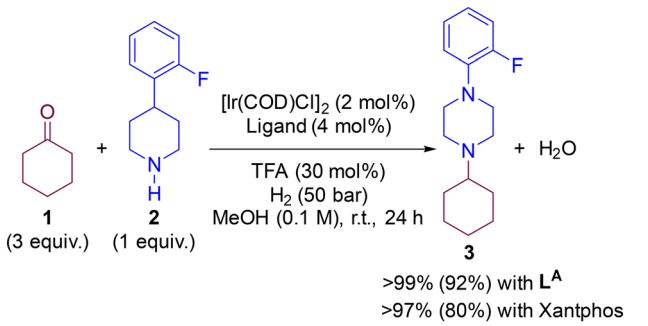

Scheme 1 Previously-developed iridium-catalysed DRA enabling formation of purely aliphatic tertiary amine **3**. Isolated yields displayed in brackets.[83]

used for the iridium and iron atoms. The BS-II basis sets were further used for single point energy optimization, in which 6-311++G(2d,p) basis sets were used for non-metallic atoms, and SDD basis sets with effective core potential were used for the iridium and iron atoms. Note that Ahlrichs' basis sets have been considered and led to very similar results (see ESI†). The contribution of thermal corrections and entropy to Gibbs free energies were obtained by using ωB97X-D/BS-I methods. The refined energies were then corrected to Gibbs energies at 298.15 K and 1 atm by using the ωB97X-D/BS-I harmonic frequencies. Calculations carried out at 50 atm instead of 1 atm led to very similar results (see ESI†).[85,90–92] The solvent effect was evaluated using SMD (density-based solution model) solvation model.[93,94] We noted that the formation of the hydrogen-bond complexes between the methanol solvent molecule and TFA derivatives are endothermic reactions, suggesting TFA derivatives cannot form stable associated complexes (see details in the ESI†). Harmonic frequency analysis is performed to verify that the optimized geometry is a minimum (no virtual frequency) or a transition state (TS, with a unique virtual frequency). All transition states were verified by employing the intrinsic reaction coordinate (IRC) procedure.[95] The cartesian coordinates of all optimized structures are presented in the ESI† (Tables S1–S3).

Formation of iminium and/or enamines

The very first step of the reaction is the condensation of ketone **1** and amine **2** assisted by TFA that may lead to the iminium **3′** and/or enamine species **3″** according to our previous hypothesis (Scheme 2).[83] To qualitatively evaluate the feasibility of the formation of the iminium **3′** and the enamine **3″**, we computed the energy landscape for the reaction of **1** with **2** in the presence of TFA (Fig. 2).

As shown in Fig. 2, the stoichiometric combination of ketone **1** and amine **2** (**A1**) binds a TFA molecule *via* hydrogen bonding between the acidic hydrogen of TFA and the carbonyl group of **1** forming the intermediate **A2** with an energy increase of +7.1 kcal mol^{-1}. The hydrogen atom from TFA is transferred to the carbonyl oxygen atom in **A2** *via* the transition state $\mathbf{TS_{A2–A3}}$, while the carbonyl carbon atom changes its hybridization from sp^2 to sp^3 in the bounding to the nearby amine nitrogen atom leading to species **A3**. The energy barrier of this intermolecular C–N coupling step is +11.6 kcal mol^{-1} and it is important to note an additional hydrogen bonding between the amine proton and an oxygen atom from TFA. Then, the TFA molecule is released to produce the aminoalcohol intermediate **A4**. In the following, **A4** rebounds to TFA proceeding to the dehydration reaction through the very accessible transition state $\mathbf{TS_{A4–3'}}$. The proton in TFA is transferred to the hydroxyl oxygen atom of the aminoalcohol **A4** together with the release of the trifluoroacetate anion and water producing the iminium **3′**. In brief, the energy span of the transition state $\mathbf{TS_{A4–3'}}$ starting from the intermediate **A3** is +13.1 kcal mol^{-1}, and the formation of the iminium species **3′** is largely exergonic by 23.5 kcal mol^{-1}. Note that a plausible reaction pathway from intermediate **A3** to iminium **3′** considering release of trifluoroacetate anion instead of TFA before reaching the transition state $\mathbf{TS_{A4–3'}}$ was highly unfavourable with an energy span of 38.8 kcal mol^{-1}, and 31.9 kcal mol^{-1} for the case in which TFA is involved in a two-fold hydrogen bonding (see Fig. S1 and S2 in the ESI†). Importantly, considering the reaction of the iminium **3′** with trifluoroacetate anion towards the formation of enamine **3″** was strongly disfavoured with a ΔG = +21.8 kcal mol^{-1}. As such, for purely aliphatic ketones and amines, the iminium intermediate **3′** is thermodynamically more favoured than the corresponding enamine **3″** intermediate. Nevertheless, it is worthy to note that under the precise reaction conditions of the catalysis the presence of free TFA is unlikely because it may instantaneously react with the amine **2** and/or the product **3**. As such, we cannot rule out a process from **3′** to **3″** *via* an acid/base reaction with the amine **2** or the product **3** acting as a base. That being said, this does not change the fact that the iminium intermediate **3′** is more favoured to form than the enamine **3″**.

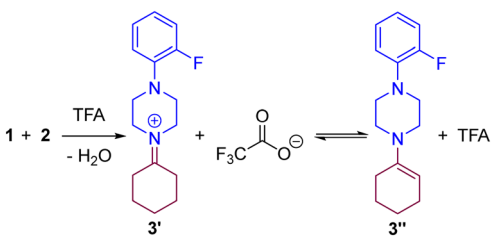

Scheme 2 Condensation of ketone **1** and amine **2** in the presence of TFA.

Iridium-catalysed hydrogenation of the iminium intermediate 3′ and catalyst regeneration with ligand $\mathbf{L^A}$

Having demonstrated the high stability of iminium **3′** over the enamine **3″**, we embarked in the DFT analysis of the hydrogenation of **3′** towards the tertiary amine **3** by an iridium complex resulting from the chelation of the Josiphos-type ligand $\mathbf{L^A}$ (Scheme 3). It is important to remind that, under the catalytic conditions, TFA is likely involved in an acid/base reaction with the product **3** at the end, leading to the protonated ammonium and triflate anion. This explains the fact that a basic work-up is required in the experimental procedure to fully recover the amine **3**. From a mechanistic point of view and based on previous reports that indicate the readily formation of penta-coordinated iridium(III) species upon combination of a P,P-chelating ligand with $[Ir(COD)Cl]_2$ under H_2 pressure,[30,96–102] we considered the iridium species **B1** (Scheme 3) as the most reasonable catalytically active ones for the hydrogenation of iminium **3′** in the presence of trifluoroacetate anion. In the following, three different

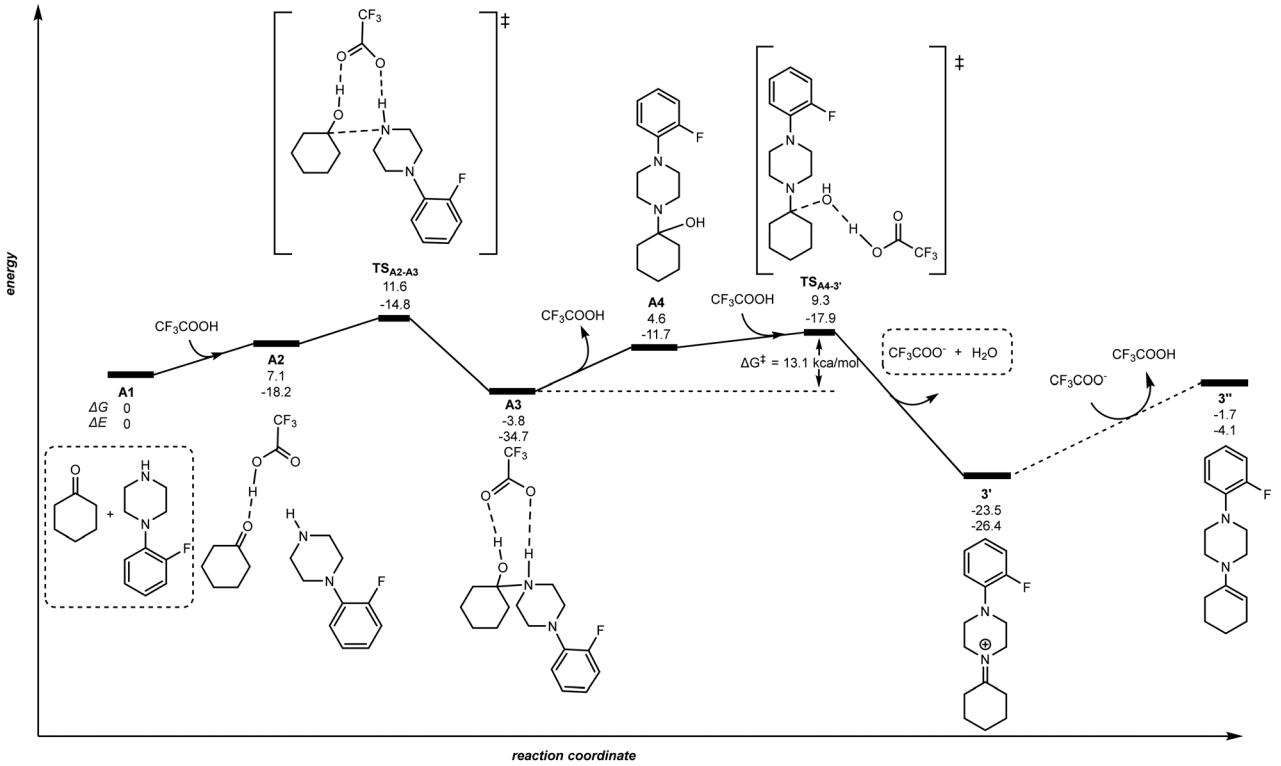

Fig. 2 Reaction pathway for the TFA-mediated condensation of ketone **1** and amine **2**. The relative Gibbs free energy (Δ*G*) and potential energy (Δ*E*) are reported in kcal mol^{-1}.

dihydride-based mechanistic pathways have been evaluated: pathways "A" (Fig. 3), "B" (Fig. 4) and "C" (Fig. 5).

Fig. 3 (pathway "A") displays the hydrogenation of **3′** considering a direct hydride/hydrogen transfer with trifluoroacetate involved in the catalyst regeneration process. First, the hydride ligand of the pentacoordinate iridium complex **B1** can be transferred to the unsaturated carbon atom of the intermediate iminium **3′** *via* the transition state $\mathbf{TS_{B1–B2}}$ with an energy span of 19.3 kcal mol^{-1}. As a result, the amine product **3** is formed. The cationic, iridium intermediate **B2** may undergo reaction with H_2 leading to a **σ**

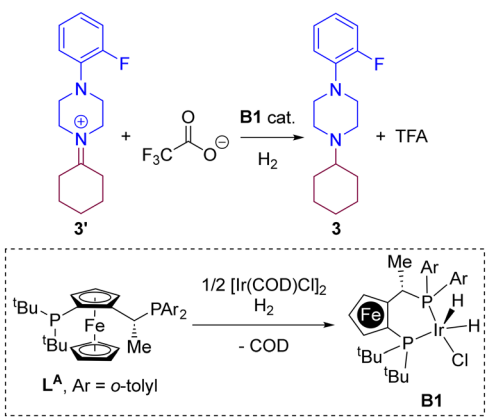

Scheme 3 Iridium-catalysed hydrogenation of iminium **3′** with the iridium **B1** catalyst.

H_2-ligated iridium species **B3** with an energy increase of 11.2 kcal mol^{-1}. The coordinated dihydrogen ligand on the iridium centre of **B3** undergoes H–H bond heterolytic cleavage thanks to the trifluoroacetate anion through the transition state $\mathbf{TS_{B3–B1}}$, thereby releasing TFA and regenerating the catalytically active iridium species **B1**. From this evaluation, the H–H bond heterocyclic cleavage *via* $\mathbf{TS_{B3–B1}}$ is the rate-determining step of the whole catalytic cycle with an energy span of 22.2 kcal mol^{-1} and the catalytic role of TFA is explained. Interestingly, it is relevant to note that these calculations did not identify any interaction between the iminium and the metal, thus ruling out any coordination to reach hexa-coordinated iridium species followed by hydride transfer.

On the other hand, we also evaluated other mechanistic scenarios, namely pathways "B" and "C" (Fig. 4 and 5, respectively). In Fig. 4 (pathway "B") we have considered the hydride/hydrogen transfer pathway with the trifluoroacetate anion coordinating to the iridium catalyst **B1** *via* a plausible hexacoordinated iridium species **C1**. The trifluoroacetate anion can coordinate to **B1**, being this process endothermic by 4.2 kcal mol^{-1}. The hydride ligand of the hexa-coordinated iridium complex **C1** is transferred to the unsaturated carbon atom of the iminium intermediate **3′** *via* the transition state $\mathbf{TS_{C1–C2}}$ with an energy span of 33.9 kcal mol^{-1}. As a result, the amine product **3** and the intermediate **C2**, with the trifluoroacetate ligand bound to iridium, are obtained. Then, the dihydrogen molecule coordinates to the iridium centre of

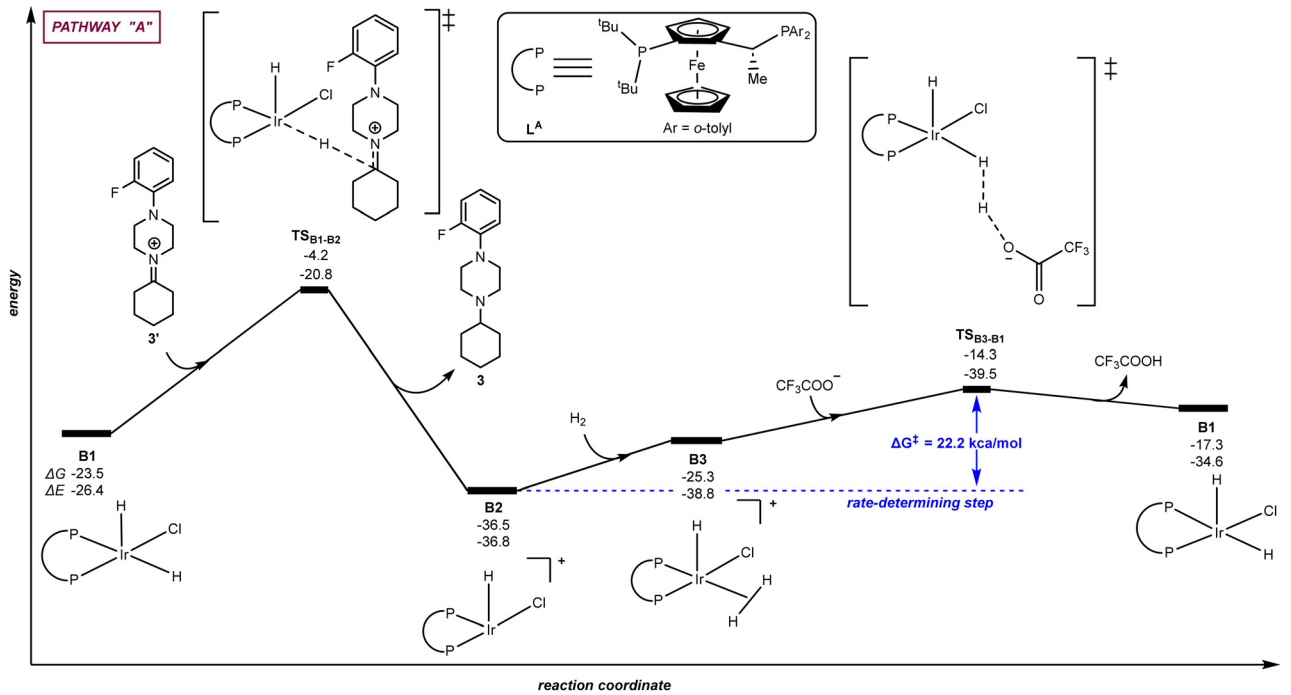

Fig. 3 Pathway "A": reaction coordinate for the hydride/hydrogen transfer pathway occurring in a penta-coordinated iridium complex **B1**. The relative Gibbs free energy (ΔG) and potential energy (ΔE) are reported in kcal mol^{-1}. P–P: diphosphane ligand L^A.

C2 to form the hexa-coordinated iridium complex (**C3**) with an energy increase of 11.0 kcal mol^{-1}. The coordinated dihydrogen ligand on the iridium centre of **C3** undergoes H–H bond heterolytic cleavage through the transition state $\mathbf{TS_{C3-B1}}$ with the trifuoroacetate ligand abstracting the hydrogen atom releasing TFA in a concerted, intramolecular manner and regenerating the catalytically active species **B1**. In this mechanistic scenario, the rate-determining step

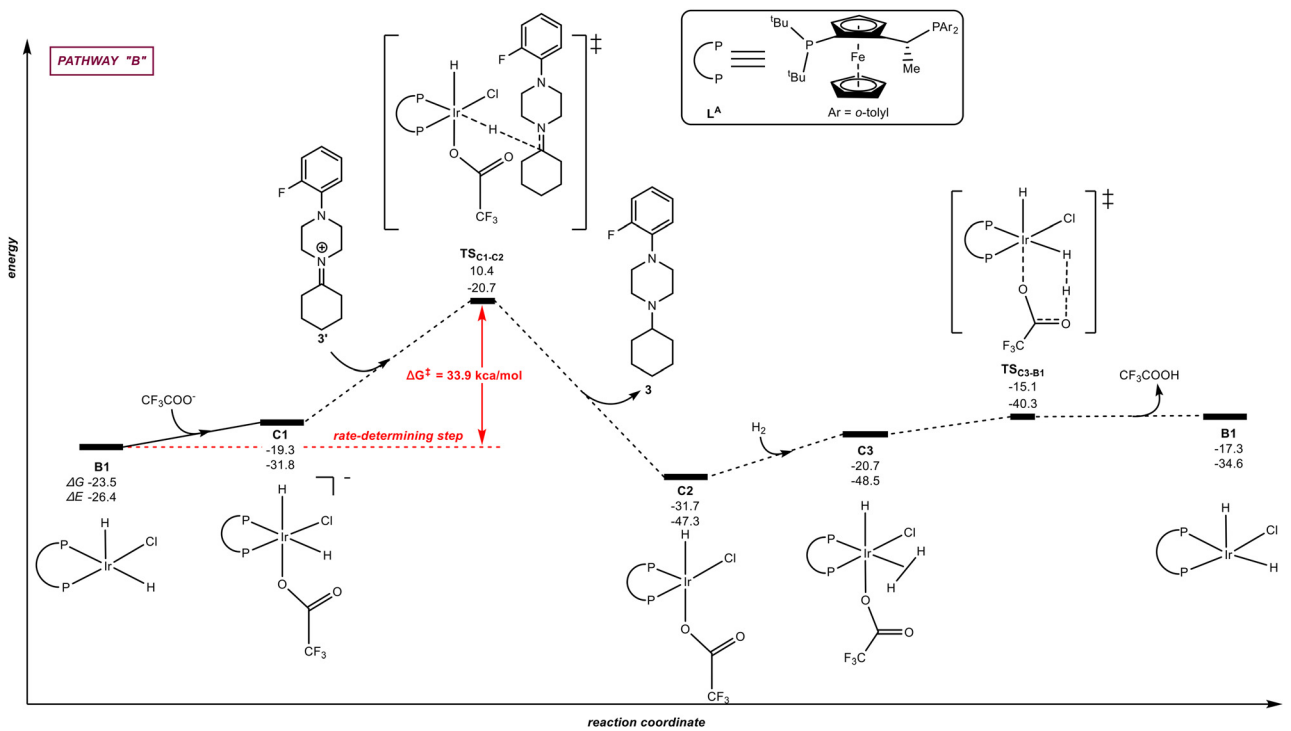

Fig. 4 Pathway "B": reaction coordinate for the trifluoroacetate-mediated, hydride/hydrogen transfer pathway occurring in a hexa-coordinated iridium complex **C1**. The relative Gibbs free energy (ΔG) and potential energy (ΔE) are reported in kcal mol^{-1}. P–P: diphosphane ligand L^A.

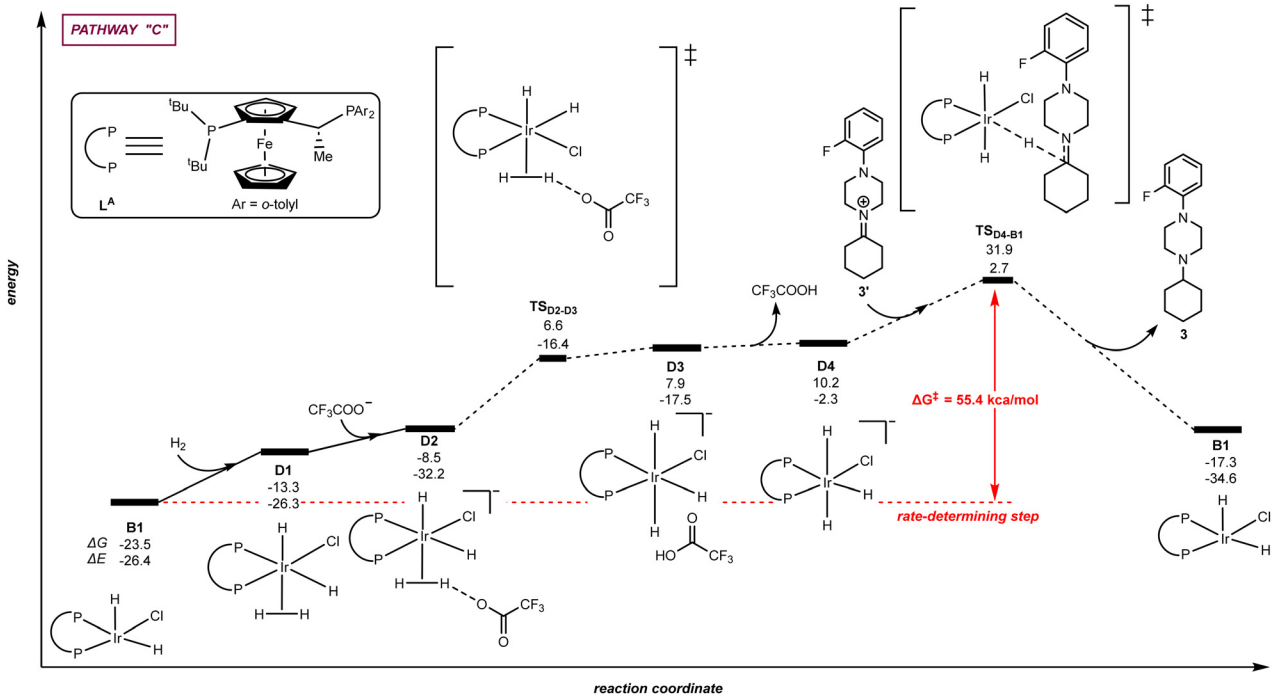

Fig. 5 Pathway "C": reaction coordinate for the trifluoroacetate-mediated, hydride/hydrogen transfer pathway occurring in a hexa-coordinated iridium complex **D1** with initial H_2 activation. The relative Gibbs free energy (ΔG) and potential energy (ΔE) are reported in kcal mol^{-1}. P–P: diphosphane ligand $\mathbf{L^A}$.

associated to the energy of $\mathbf{TS_{C1–C2}}$ (Fig. 4) is higher than that of $\mathbf{TS_{B3–B1}}$ (Fig. 3) by 11.7 kcal mol^{-1}, indicating that the trifluoroacete-mediated pathway "B" is unlikely using the Josiphos-type ligand $\mathbf{L^A}$.

Alternatively to the trifluoroacetate-mediated pathway above-described in Fig. 4, we envisioned a different mechanistic scenario in which H_2 activation occurs at the iridium species **B1** leading to a hexa-coordinated iridium species with the trifluoroacetate anion behaving as an external base without coordination to iridium, namely pathway "C" (Fig. 5). More precisely, the DFT-computed pathway "C" started with the reaction of **B1** with H_2 in which the H_2 molecule coordinates in a **σ** manner to the iridium centre of **B1** forming the hexa-coordinated species **D1** with an energy increase of +10.2 kcal mol^{-1}. In the presence of trifluoroacetate anion, the coordinated dihydrogen ligand on the iridium centre of **D1** undergoes H–H bond heterolytic cleavage *via* intermediate **D2** and through the transition state $\mathbf{TS_{D2–D3}}$. A hydrogen atom is abstracted by the trifluoroacetate anion forming TFA as well as the anionic iridium intermediate **D4**. Subsequently, the hydride ligand of the hexa-coordinated iridium intermediated **D4** can be transferred to the unsaturated carbon atom of the iminium intermediate **3′** *via* the transition state $\mathbf{TS_{D4–B1}}$ with an energy barrier of +21.7 kcal mol^{-1} while regenerating the catalyst **B1**. The energy span for the hydride transfer transition state $\mathbf{TS_{D4–B1}}$ is very high (+55.4 kcal mol^{-1}), strongly suggesting that this pathway is not accessible in the experimental conditions in which the catalysis occurs at room temperature. As such, from the three different mechanistic scenarios evaluated (Fig. 3–5), the most plausible one for the iridium-catalysed hydrogenation pathway using the ligand $\mathbf{L^A}$ is *via* the iridium penta-coordinated pathway "A" displayed in Fig. 3 (*vide supra*).

Iridium-catalysed hydrogenation of the iminium intermediate 3′ and catalyst regeneration with Xantphos ligand

Because similar efficiency is found with the Josiphos-type ligand $\mathbf{L^A}$ and Xantphos (Scheme 1), we were curious to see which pathway ("A", "B" or "C") was more favoured with Xantphos starting from the homologous catalytically active iridium species to **B1**, namely **E1** [(Xantphos)Ir(H)$_2$(Cl)]. Fig. 6 displays the reaction trajectory for the hydrogenation of the iminium **3′** starting from **E1** *via* a penta-coordinated iridium intermediate (right, pathway "A") and *via* a hexa-coordinated iridium intermediate **F1** (left, pathway "B"). The rate-determining step for pathway "A" is placed at +28.5 kcal mol^{-1} whereas the one for pathway "B" is at +27.4 kcal mol^{-1}. This difference might be relevant enough for a reaction occurring at room temperature, especially considering that the key transition state ($\mathbf{TS_{F1–F2}}$) is reached *via* the intermediate **F1** that is higher in energy than **E1**. Comparing both pathways after the rate-determining step, it is evident that intermediate **F2** is more accessible than **E2**, leading to a mild trajectory for the following hydrogen activation step as well as providing an affordable driving force for the previous

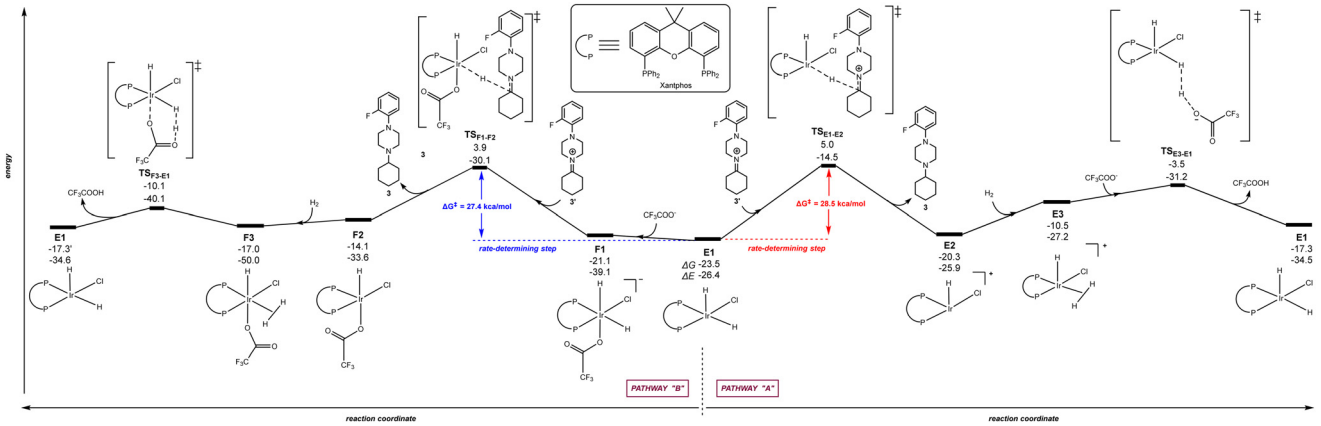

Fig. 6 Reaction coordinate for the hydride/hydrogen transfer pathway occurring in a penta-coordinated iridium complex **E1** (pathway "A", right - unfavourable) and reaction coordinate for the trifluoroacetate-mediated, hydride/hydrogen transfer pathway occurring in a hexa-coordinated iridium complex **F1** (pathway "B", left - favourable). The relative Gibbs free energy (ΔG) and potential energy (ΔE) are reported in kcal mol^{-1}. P–P: diphosphane ligand Xantphos.

hydride addition step. Overall, the rate-determining step for the iridium-catalysed hydrogenation of **3′** using Xantphos appears to follow the hexa-coordinated pathway "B" and the scenario is reversed considering pathways "A" and "B" with the Josiphos-type ligand $\mathbf{L^A}$. Note that the pathway "C" with Xantphos, which comprised initial H_2 activation followed by trifluoroacetate-mediated, hydride/hydrogen transfer pathway occurring in an hexa-coordinated iridium complex led to a much higher energy barrier (+53.6 kcal mol^{-1}) for the rate-determining step (see details in Fig. S3 in the ESI†), similarly as found in Fig. 5 for ligand $\mathbf{L^A}$, thereby ruling out this reaction pathway for Xantphos as well. Consequently, the Xantphos ligand, which is known to give rise to metal complexes with very large bite-angles[103–105] and its phosphorus atoms are of different steric and electronic nature compared to Josiphos-type ligand $\mathbf{L^A}$, is a truly convenient and affordable ligand for the iridium-catalysed DRA between both aliphatic amines and aliphatic ketones.

Attempts of predicting the iridium-catalysed hydrogenation of the iminium intermediate 3′ with catalysts based on Josiphos-type ligand $\mathbf{L^B}$ and BIBOP-type ligand $\mathbf{L^C}$

Based on the above-described findings, we wondered whether other type of Josiphos-type ligand, such as $\mathbf{L^B}$ that bears different substitution patterns in the phosphorus atoms compared to $\mathbf{L^A}$, could eventually be used for this transformation. Moreover, due to the fact that Xantphos, in which the phosphorus atoms are wide apart over six chemical bonds, typically leads to metal complexes with a relatively large bite angle,[103–105] we aimed at comparing it with a ligand whose metal complexes display a small bite angle, such as BIBOP-type ligand $\mathbf{L^C}$,[106–110] with only three chemical bonds separating the two chelating phosphorus atoms (Scheme 4). We reasoned that these two ligands can give rise to catalytically active **G1** and **I1** species (Scheme 4), respectively, which we considered as the initial point for the calculations involving hydrogenation of the iminium **3′** towards amine **3**.

The calculations were carried out following the three pathways "A", "B" and "C" above-considered for $\mathbf{L^A}$ and Xantphos, respectively. Fig. 7 and 8 displays the reaction pathways "A" and "B" for $\mathbf{L^B}$ and $\mathbf{L^C}$, respectively. Note that the pathway "C" with $\mathbf{L^B}$ or $\mathbf{L^C}$, which comprised initial H_2 activation followed by trifluoroacetate-mediated, hydride/hydrogen transfer pathway occurring in an hexa-coordinated iridium complex (equivalent to Fig. 5, *vide supra*) led to a much higher energy barrier (+55.2 kcal mol^{-1} for $\mathbf{L^B}$ and +40.0 kcal mol^{-1} for $\mathbf{L^C}$) for the rate-determining step (see details in Fig. S4 and S5 in the ESI†), similarly as found for ligands $\mathbf{L^A}$ and Xantphos, thus ruling out this reaction pathway for $\mathbf{L^B}$ and $\mathbf{L^C}$ too.

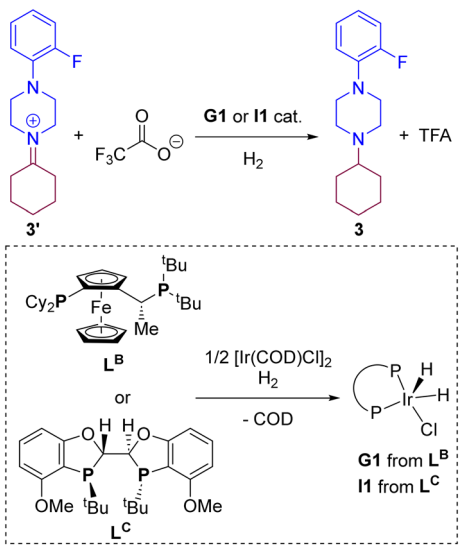

Scheme 4 Iridium-catalysed hydrogenation of iminium **3′** with the iridium **G1** and **I1** catalysts derived from ligands $\mathbf{L^B}$ and $\mathbf{L^C}$ considered for DFT computations.

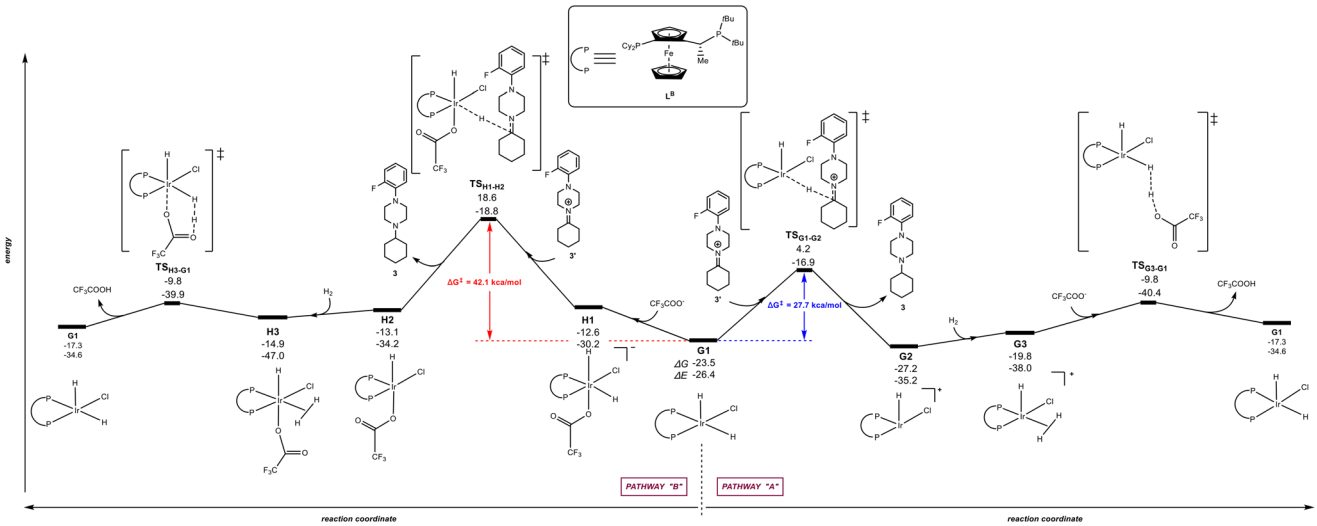

Fig. 7 Reaction coordinate for the hydride/hydrogen transfer pathway occurring in a penta-coordinated iridium complex **G1** (pathway "A", right) and reaction coordinate for the trifluoroacetate-mediated, hydride/hydrogen transfer pathway occurring in a hexa-coordinated iridium complex **H1** (pathway "B", left). The relative Gibbs free energy (ΔG) and potential energy (ΔE) are reported in kcal mol^{-1}. P–P: diphosphane ligand $\mathbf{L^B}$.

The Josiphos-type ligand $\mathbf{L^B}$ prefers to follow the pathway "A" rather than the pathway "B" (Fig. 6) as it was also found previously for $\mathbf{L^A}$ with the same ferrocene backbone. However, the rate-determining step for the reaction pathway "A" is 5.5 kcal mol^{-1} higher in energy that the one obtained with $\mathbf{L^A}$ (27.7 kcal mol^{-1} *vs.* 22.2 kcal mol^{-1}). In agreement with a higher energetic profile associated to $\mathbf{L^B}$, the rate-determining step for $\mathbf{L^B}$ in the pathway "B" reached the value of 42.1 kcal mol^{-1} (Fig. 7), which is 8.2 kcal mol^{-1} higher in energy than the one observed for pathway "B" using ligand $\mathbf{L^A}$. Consequently, $\mathbf{L^B}$ appears to be less efficient than $\mathbf{L^A}$ but similar to Xantphos, which featured a rate-determining step at a comparable 27.4 kcal mol^{-1} although *via* the pathway "B" (Fig. 6).

Regarding the behaviour of $\mathbf{L^D}$, we found that both reaction pathways "A" and "B" are energetically accessible with rate-determining steps associated to 19.0 kcal mol^{-1} and 19.4 kcal mol^{-1}, respectively (Fig. 8). These values are very similar to those observed with $\mathbf{L^A}$ considering the reaction pathway "A" (Fig. 3). Interestingly, the rate-determining step for pathway "B" with ligand $\mathbf{L^B}$ correspond to the catalyst regeneration step and not the hydrogen/hydride transfer to the substrate, in stark contrast with the other three ligands analysed here. These findings indicate that, in principle, ligands $\mathbf{L^B}$ and $\mathbf{L^C}$, should promote the iridium-catalysed DRA between aliphatic amines. However, we reported that when using 2-butanone instead of cyclohexanone as ketone for the reaction with the amine **2**, its conversion and the isolated yields of the corresponding tertiary amine product decreased significantly compared to $\mathbf{L^A}$ and Xantphos.[83]

To evaluate the predicted behaviour of $\mathbf{L^B}$ and $\mathbf{L^C}$, we performed experimentally the iridium-catalysed DRA between

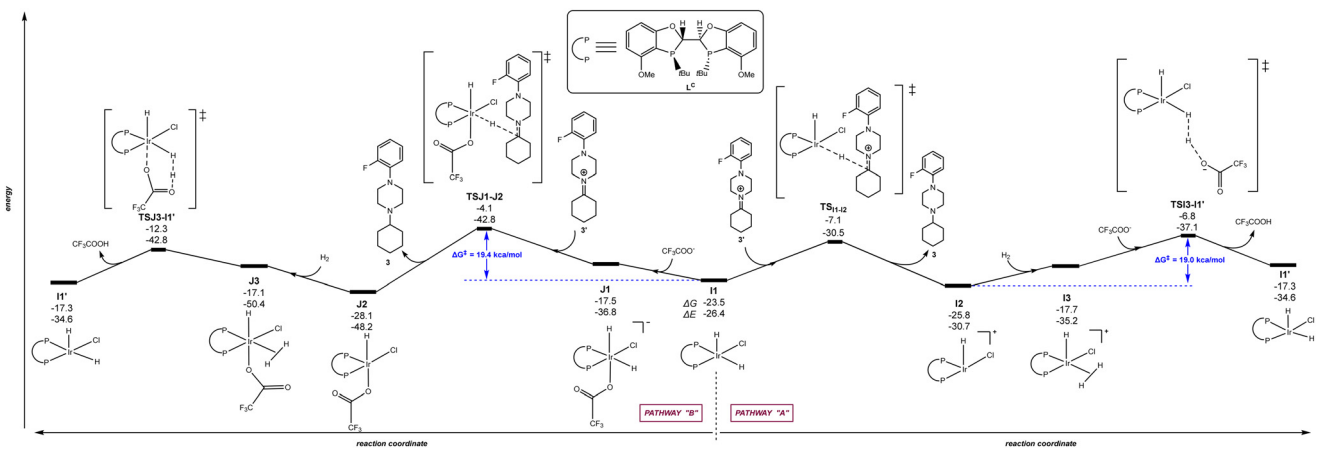

Fig. 8 Reaction coordinate for the hydride/hydrogen transfer pathway occurring in a penta-coordinated iridium complex **I1** (pathway "A", right) and reaction coordinate for the trifluoroacetate-mediated, hydride/hydrogen transfer pathway occurring in a hexa-coordinated iridium complex **J1** (pathway "B", left). The relative Gibbs free energy (ΔG) and potential energy (ΔE) are reported in kcal mol^{-1}. P–P: diphosphane ligand $\mathbf{L^C}$.

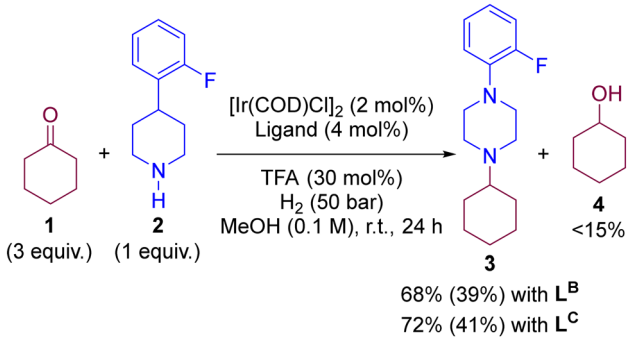

Scheme 5 Experimental results for the iridium-catalysed DRA enabling formation of purely aliphatic tertiary amine **3** using ligands $\mathbf{L^B}$ and $\mathbf{L^C}$, respectively. Isolated yields displayed in brackets.

Table 1 Summary regarding the rate-determining step *versus* the activity and selectivity of the iridium-coordinated ligands

	Conv.	Yield	Yield	Rate-determining step (kcal mol^{-1})		
Ligand	**2** (%)	**3** (%)	**4** (%)	Path A	Path B	Path C
$\mathbf{L^A}$	>99	92	0	22.2	33.9	55.4
Xantphos	>97	80	0	28.5	27.4	53.6
$\mathbf{L^B}$	68	39	<15	27.7	42.1	55.2
$\mathbf{L^C}$	72	41	<15	19.0	19.4	40.0

1 and **2** under H_2 atmosphere and methanol solvent at room temperature using catalytic amounts of TFA (30 mol%). Note that the reaction conditions are identical to those used with $\mathbf{L^A}$ and Xantphos, respectively, in Scheme 1 (*vide supra*). After 24 hours of reaction, the conversions using $\mathbf{L^B}$ and $\mathbf{L^C}$ were around 70% with the tertiary amine **3** being isolated in yields close to 40% (Scheme 5). Importantly, we noted the formation of the cyclohexanol side-product **4** originating form a formal hydrogenation of the ketone **1** in yields around to 15% according to GC-MS analysis (see ESI† for details). Consequently, the performance of $\mathbf{L^B}$ and $\mathbf{L^C}$ for DRA predicted by DFT calculations was in competition with a ketone hydrogenation reaction, which is not the case of Josiphos-type ligand $\mathbf{L^A}$ and Xantphos. Overall, the ligands $\mathbf{L^B}$ and $\mathbf{L^C}$ are not as competent as $\mathbf{L^A}$ and Xantphos for the DRA between aliphatic ketones and amines. A summary of the key observations regarding the rate-determining step in each pathway *versus* the reactivity in catalysis is provided in Table 1. Finally, we envisioned to analyse by NBO analysis the key DFT-computed key transitions states involving the hydride transfer step from the metal to the substrate (Fig. S37 in the ESI†). It is found that the electronegativities of hydrides and the steric hindrance can well account for the computed energy barriers of the hydride transfer steps.

Conclusions

In conclusion, by means of state-of-the-art computation calculations at the DFT level, we have demonstrated that the iridium-catalysed DRA reaction between aliphatic ketones and aliphatic amines follows very different mechanistic trajectories depending on the nature of the ligand.[111,112] In particular, the already experimentally identified Josiphos-type ligands $\mathbf{L^A}$ and Xantphos follow very different reaction pathways. Whilst $\mathbf{L^A}$ favours the hydride/hydrogen transfer pathway occurring in a penta-coordinated iridium (pathway "A"), the large bite-angle diphosphane Xantphos is more adapted to the trifluoroacetate-mediated, hydride/hydrogen transfer pathway occurring in a hexa-coordinated iridium complex (pathway "B"). With the aim of predicting the catalytic outcome, the calculations using Josiphos-type ligand $\mathbf{L^B}$ and the small bite-angle BIBOP-type ligand $\mathbf{L^C}$ led to rather counterintuitive findings with both ligands appearing suitable for the iridium-catalysed DRA although *via* different rate-determining steps. However, the experimental results shown non-negligible formation of ketone hydrogenation as a side-reaction. As such, ligands $\mathbf{L^B}$ and $\mathbf{L^C}$ are engaged in undesired processes, thereby underperforming $\mathbf{L^A}$ and Xantphos for iridium-catalysed DRA. In addition, we have shown that the iminium intermediate is more stable than the corresponding enamine for the case of purely aliphatic substrates, which is of relevance for evaluating metal-catalysed DRA or other type of (asymmetric) hydrogenations. Furthermore, we demonstrate and highlight the complex mechanistic scenarios that should have to be considered for metal-catalysed hydrogen-mediated organic transformations.

Data availability statement

The data supporting this article have been included as part of the ESI.†

Conflicts of interest

There are no conflicts to declare.

Acknowledgements

Financial support from the CNRS, University of Rennes and Janssen Pharmaceutica N.V. (Johnson & Johnson) is acknowledged. The work in Hebei University is supported by the National Natural Science Foundation of China (22373030), the Excellent Youth Research Innovation Team of Hebei University (QNTD202406), and the Innovation Team Project of Hebei University (IT2023C01).

Notes and references

1 P. W. N. M. van Leeuwen, *Homogeneous Catalysis: Understanding the Art*, Kluwer, Dordrecht, 2004.
2 J. F. Hartwig, *Organotransition Metal Chemistry: From Bonding to Catalysis*, University Science Books, Sausalito, 2009.
3 M. Beller and C. Bolm, *Transition Metals for Organic Synthesis*, Wiley-VCH, Weinheim, 2004.

4 D. Selent and D. Heller, In-Situ Techniques for Homogeneous Catalysis in *Catalysis: From Principles to Applications*, ed. M. Beller, A. Renken and R. A. van Santen, Wiley-VCH, Weinheim, 2012, pp. 465–490.
5 M. Garland, *Catal. Today*, 2010, **155**, 266–270.
6 A. Haynes, The Use of High Pressure Infrared Spectroscopy to Study Catalytic Mechanisms in *Mechanisms in Homogeneous Catalysis*, ed. B. Heaton, Wiley-VCH, Weinheim, Germany, 2005, pp. 107–150.
7 N. J. Beach, S. M. M. Knapp and C. R. Landis, *Rev. Sci. Instrum.*, 2015, **86**, 104101–104109.
8 A. C. Brezny and C. R. Landis, *ACS Catal.*, 2019, **9**, 2501–2513.
9 A. Duchowny, S. A. Ortiz Restrepo, M. Adams, R. Thelen and A. Adams, *Analyst*, 2022, **147**, 3827–3832.
10 I. T. Horvath and J. M. Millar, *Chem. Rev.*, 1991, **91**, 1339–1351.
11 N. R. Jaegers, K. T. Mueller, Y. Wang and J. Z. Hu, *Acc. Chem. Res.*, 2020, **53**, 611–619.
12 J. M. Dreimann, E. Kohls, H. F. W. Warmeling, M. Stein, L. F. Guo, M. Garland, T. N. Dinh and A. J. Vorholt, *ACS Catal.*, 2019, **9**, 4308–4319.
13 E. Groppo, S. Rojas-Buzo and S. Bordiga, *Chem. Rev.*, 2023, **123**, 12135–12169.
14 T. K. Slot, N. R. Shiju and G. Rothenberg, *Angew. Chem., Int. Ed.*, 2019, **58**, 17273–17276.
15 O. Diebolt, P. W. N. M. van Leeuwen and P. C. J. Kamer, *ACS Catal.*, 2012, **2**, 2357–2370.
16 V. Butera, *Phys. Chem. Chem. Phys.*, 2024, **26**, 7950–7970.
17 F. Maseras and A. Lledós, *Computational Modeling of Homogeneous Catalysis*, Kluwer Academic Publishers, Dordrecht, The Netherlands, 2002.
18 K. Morokuma and D. G. Musaev, in *Computational Modeling for Homogeneous and Enzymatic Catalysis: A Knowledge-Base for Designing Efficient Catalysts*, Wiley-VCH, Weinheim, 2008.
19 A. V. Kalikadien, A. Mirza, A. N. Hossaini, A. Sreenithya and E. A. Pidko, *ChemPlusChem*, 2024, **89**, e202300702.
20 M. Foscato and V. R. Jensen, *ACS Catal.*, 2020, **10**, 2354–2377.
21 J. Lan, X. Li, Y. Yang, X. Zhang and L. W. Chung, *Acc. Chem. Res.*, 2022, **55**, 1109–1123.
22 W. Yang, G. A. Filonenko and E. A. Pidko, *Chem. Commun.*, 2023, **59**, 1757–1768.
23 A. Lledós, *Eur. J. Inorg. Chem.*, 2021, 2547–2555.
24 Y. Musashi and S. Sakaki, *J. Am. Chem. Soc.*, 2002, **124**, 7588–7603.
25 Y. Luo, Z. Huang, Z. Chen, Z. Xu, J. Meng, H.-Y. Li, Q. Meng and D. Tang, *J. Org. Chem.*, 2020, **85**, 11626–11634.
26 J. Faiges, C. Borràs, I. M. Pastor, O. Pàmies, M. Besora and M. Diéguez, *Organometallics*, 2021, **40**, 3424–3435.
27 A. M. Krieger, P. Kuliaev, F. Q. A. Hall, D. Sun and E. A. Pidko, *J. Phys. Chem. C*, 2020, **124**, 26990–26998.
28 P. Chakraborty, B. Sundararaju, E. Manoury and R. Poli, *ACS Catal.*, 2021, **11**, 11906–11920.
29 R. P. Dias and W. R. Rocha, *Organometallics*, 2011, **30**, 4257–4268.
30 C.-X. Cui, H. Chen, S.-J. Li, T. Zhang, L.-B. Qu and Y. Lan, *Coord. Chem. Rev.*, 2020, **412**, 213251.
31 B. Liu, N. Huang, Y. Wang, X. Lan and T. Wang, *Chem. Eng. J.*, 2022, **441**, 136101.
32 M. Besora and F. Maseras, *Adv. Catal.*, 2021, **68**, 385–426.
33 S. A. Decker and T. R. Cundari, *Organometallics*, 2001, **20**, 2827–2841.
34 S. S. Nurttila, P. R. Linnebank, T. Krachko and J. N. H. Reek, *ACS Catal.*, 2018, **8**, 3469–3488.
35 S. Zhang, Z. Li, H. Qi, Y. Zhao, Y. Tang, A. Liu, M. Pu and M. Lei, *Dalton Trans.*, 2024, **53**, 6660–6666.
36 J. Fang, Z.-Q. Wang, X. Wei, Y. Ma, H. Gong, X.-Q. Gong and Z. Hou, *ACS Sustainable Chem. Eng.*, 2021, **9**, 13256–13267.
37 M. Cheong, R. Schmid and T. Ziegler, *Organometallics*, 2000, **19**, 1973–1982.
38 F. León, A. Comas-Vives, E. Álvarez and A. Pizzano, *Catal. Sci. Technol.*, 2021, **11**, 2497–2511.
39 M. Sterle, M. Huš, M. Lozinšek, A. Zega and A. E. Cotman, *ACS Catal.*, 2023, **13**, 6242–6248.
40 T. Irrgang and R. Kempe, *Chem. Rev.*, 2020, **120**, 9583–9674.
41 O. I. Afanasyev, E. Kuchuk, D. L. Usanov and D. Chusov, *Chem. Rev.*, 2019, **119**, 11857–11911.
42 V. I. Tararov, R. Kadyrov, T. H. Riermeier and A. Börner, *Chem. Commun.*, 2000, 1867–1868.
43 K. O. Biriukov, M. M. Vinogradov, O. I. Afanasyev, D. V. Vasilyev, A. A. Tsygankov, M. Godovikova, Y. V. Nelyubina, D. A. Loginov and D. Chusov, *Catal. Sci. Technol.*, 2021, **11**, 4922–4930.
44 R. R. Thakore, B. S. Takale, G. Casotti, E. S. Gao, H. S. Jin and B. H. Lipshutz, *Org. Lett.*, 2020, **22**, 632–6329.
45 *Green Chemistry: Theory and Practice*, ed. P. T. Anastas and J. C. Warner, Oxford University Press, Oxford, 1998.
46 B. Trost, *Science*, 1991, **254**, 1471–1477.
47 R. Noyori, *Nat. Chem.*, 2009, **1**, 5–6.
48 K. Alfonsi, J. Colberg, P. J. Dunn, T. Fevig, S. Jennings, T. A. Johnson, H. P. Kleine, C. Knight, M. A. Nagy, D. A. Perry and M. Stefaniak, *Green Chem.*, 2008, **10**, 31–36.
49 R. A. Sheldon, *ACS Sustainable Chem. Eng.*, 2018, **6**, 32–48.
50 Z. Zhang, T. Ikeda, H. Murayama, T. Honma, M. Tokunaga and Y. Motoyama, *Chem. – Asian J.*, 2022, **17**, e20210124.
51 F. Kliuev, A. Kuznetsov, O. I. Afanasyev, S. A. Runikhina, E. Kuchuk, E. Podyacheva, A. A. Tsygankov and D. Chusov, *Org. Lett.*, 2022, **24**, 7717–7721.
52 E. Podyacheva, O. I. Afanasyev, A. A. Tsygankov, M. Makarova and D. Chusov, *Synthesis*, 2019, **51**, 2667–2677.
53 B. Li, J.-B. Sortais and C. Darcel, *RSC Adv.*, 2016, **6**, 57603–57625.
54 *Reductions by the Alumino- and Borohydrides in Organic Synthesis*, ed. J. Seyden-Penne, Wiley, New York, 2nd edn, 1997.
55 A. F. Abdel-Magid and S. J. Mehrman, *Org. Process Res. Dev.*, 2006, **10**, 971–1031.
56 A. F. Abdel-Magid, K. G. Carson, B. D. Harris, C. A. Maryanoff and R. D. Shah, *J. Org. Chem.*, 1996, **61**, 3849–3862.

57 Q. Zou, F. Liu, T. Zhao and X. Hu, *Chem. Commun.*, 2021, **57**, 8588–8591.
58 *Amines: Synthesis, Properties and Applications*, ed. S. A. Lawrence, Cambridge University Press, Cambridge, 2004.
59 S. D. Roughley and A. M. Jordan, *J. Med. Chem.*, 2011, **54**, 3451–3479.
60 V. Froidevaux, C. Negrell, S. Caillol, J.-P. Pascault and B. Boutevin, *Chem. Rev.*, 2016, **116**, 14181–14224.
61 R. V. Jagadeesh, K. Murugesan, A. S. Alshammari, H. Neumann, M.-M. Pohl, J. Radnik and M. Beller, *Science*, 2017, **358**, 326–332.
62 A. Zanasi, M. Mazzolini and A. Kantar, *Multidiscip. Respir. Med.*, 2017, **12**, 7.
63 Y. Hirayama, M. Ikunaka and J. Matsumoto, *Org. Process Res. Dev.*, 2005, **9**, 30–38.
64 *Concise Dictionary of Pharmacological Agents: Properties and Synonyms*, ed. I. K. Morton and J. M. Hall, Springer, Dordrecht, 1999.
65 Y. Tian, L. Hu, Y.-Z. Wang, X. Zhang and Q. Yin, *Org. Chem. Front.*, 2021, **8**, 2328–2342.
66 S. H. Gilbert, S. Tin, J. A. Fuentes, T. Fanjul and M. L. Clarke, *Tetrahedron*, 2021, **80**, 131863.
67 S. Yuan, G. Gao, L. Wang, C. Liu, L. Wan, H. Huang, H. Geng and M. Chang, *Nat. Commun.*, 2020, **11**, 621.
68 J. H. Schrittwieser, S. Velikogne and W. Kroutil, *Adv. Synth. Catal.*, 2015, **357**, 1655–1685.
69 R. Kumar, M. J. Karmilowicz, D. Burke, M. P. Burns, L. A. Clark, C. G. Connor, E. Cordi, N. M. Do, K. M. Doyle, S. Hoagland, C. A. Lewis, D. Mangan, C. A. Martinez, E. L. McInturff, K. Meldrum, R. Pearson, J. Steflik, A. Rane and J. Weaver, *Nat. Catal.*, 2021, **4**, 775–782.
70 S. Simić, E. Zukić, L. Schmermund, K. Faber, C. K. Winkler and W. Kroutil, *Chem. Rev.*, 2022, **122**, 1052–1126.
71 Z. Gao, J. Liu, H. Huang, H. Geng and M. Chang, *Angew. Chem., Int. Ed.*, 2021, **60**, 27307–27311.
72 J.-H. Xie, S.-F. Zhu and Q.-L. Zhou, *Chem. Rev.*, 2011, **111**, 1713–1760.
73 Z. Zhang, N. A. Butt and W. Zhang, *Chem. Rev.*, 2016, **116**, 14769–14827.
74 K. Källström, I. Munslow and P. G. Andersson, *Chem. – Eur. J.*, 2006, **12**, 3194–3200.
75 N. Fleury-Brégeot, V. de la Fuente, S. Castillón and C. Claver, *ChemCatChem*, 2010, **2**, 1346–1371.
76 R. A. A. Abdine, G. Hedouin, F. Colobert and J. Wencel-Delord, *ACS Catal.*, 2021, **11**, 215–247.
77 A. Fabrello, A. Bachelier, M. Urrutigoïty and P. Kalck, *Coord. Chem. Rev.*, 2010, **254**, 273–287.
78 N. U. D. Reshi, V. B. Saptal, M. Beller and J. K. Bera, *ACS Catal.*, 2021, **11**, 13809–13837.
79 S. H. Gilbert, V. Viseur and M. L. Clarke, *Chem. Commun.*, 2019, **55**, 6409–6412.
80 H.-U. Blaser, H.-P. Buser, H.-P. Jalett, B. Pugin and F. Spindler, *Synlett*, 1999, **S1**, 867–868.
81 P. Cheruku, T. L. Church, A. Trifonova, T. Wartmann and P. G. Andersson, *Tetrahedron*, 2008, **49**, 7290–7293.
82 Z. Wu, S. Du, G. Gao, W. Yang, X. Yang, H. Huang and M. Chang, *Chem. Sci.*, 2019, **10**, 4509–4514.
83 M. Jouffroy, T.-M. Nguyen, M. Cordier, M. Blot, T. Roisnel and R. Gramage-Doria, *Chem. – Eur. J.*, 2022, **28**, e202201078.
84 R. Xie, H. Zhou, H. Lu, Y. Mu, G. Xu and M. Chang, *Org. Lett.*, 2022, **24**, 9033–9037.
85 I. Borthakur, S. Nandi, Y. Bilora, B. Sadhu and S. Kundu, *ACS Catal.*, 2024, **14**, 5847–5857.
86 X.-Y. Lv and R. Martin, *Org. Lett.*, 2023, **25**, 3750–3754.
87 R. Xie, C. Liu, R. Lin, R. Zhang, H. Huang and M. Chang, *Org. Lett.*, 2022, **24**, 5646–5650.
88 J. D. Chai and M. Head-Gordon, *Phys. Chem. Chem. Phys.*, 2008, **10**, 6615–6620.
89 M. J. Frisch, G. W. Trucks, H. B. Schlegel, G. E. Scuseria, M. A. Robb, J. R. Cheeseman, G. Scalmani, V. Barone, B. Mennucci, G. A. Petersson, H. Nakatsuji, M. Caricato, X. Li, H. P. Hratchian, A. F. Izmaylov, J. Bloino, G. Zheng, J. L. Sonnenberg, M. Hada, M. Ehara, K. Toyota, R. Fukuda, J. Hasegawa, M. Ishida, T. Nakajima, Y. Honda, O. Kitao, H. Nakai, T. Vreven, J. A. Montgomery Jr., J. E. Peralta, F. Ogliaro, M. Bearpark, J. J. Heyd, E. Brothers, K. N. Kudin, V. N. Staroverov, R. Kobayashi, J. Normand, K. Raghavachari, A. Rendell, J. C. Burant, S. S. Iyengar, J. Tomasi, M. Cossi, N. Rega, J. M. Millam, M. Klene, J. E. Knox, J. B. Cross, V. Bakken, C. Adamo, J. Jaramillo, R. Gomperts, R. E. Stratmann, O. Yazyev, A. J. Austin, R. Cammi, C. Pomelli, J. W. Ochterski, R. L. Martin, K. Morokuma, V. G. Zakrzewski, G. A. Voth, P. Salvador, J. J. Dannenberg, S. Dapprich, A. D. Daniels, O. Farkas, J. B. Foresman, J. V. Ortiz, J. Cioslowski and D. J. Fox, *Gaussian 09, revision B.01*, Gaussian, Inc., Wallingford, CT, 2009.
90 G. J. Baker, A. J. P. White, I. J. Casely, D. Grainger and M. R. Crimmin, *J. Am. Chem. Soc.*, 2023, **145**, 7667–7674.
91 K. H. Hopmann, *Chem. – Eur. J.*, 2015, **21**, 10020–10030.
92 H. Li, M. Wen and Z.-X. Wang, *Inorg. Chem.*, 2012, **51**, 5716–5727.
93 C. J. C. A. V. Marenich and D. G. Truhlar, *J. Phys. Chem. B*, 2009, **113**, 6378–6396.
94 J. Tomasi and M. Persico, *Chem. Rev.*, 1994, **94**, 2027–2094.
95 T. Tsutsumi, Y. Ono, Z. Arai and T. Taketsugu, *J. Chem. Theory Comput.*, 2018, **14**, 4263–4270.
96 K. H. Hopmann and A. Bayer, *Organometallics*, 2011, **30**, 2483–2497.
97 J. M. Mwansa and M. I. Page, *Catal. Sci. Technol.*, 2020, **10**, 590–612.
98 K. H. Hopmann and A. Bayer, *Coord. Chem. Rev.*, 2014, **268**, 59–82.
99 R. Crabtree, *Acc. Chem. Res.*, 1979, **12**, 331–337.
100 V. R. Landaeta, B. K. Muñoz, M. Peruzzini, V. Herrera, C. Bianchini and R. A. Sánchez-Delgado, *Organometallics*, 2006, **25**, 403–409.
101 M. Martín, E. Sola, S. Tejero, J. L. Andrés and L. A. Oro, *Chem. – Eur. J.*, 2006, **12**, 4043–4056.

102 Y. Huang, S. Liu, Y. Liu, Y. Chen, M. Weisel, R. T. Williamson, I. W. Davies and X. Zhang, *Tetrahedron*, 2018, **74**, 2182–2190.
103 P. Dierkes and P. W. N. M. van Leeuwen, *J. Chem. Soc., Dalton Trans.*, 1999, 1519–1529.
104 M.-N. Birkholz, Z. Freixa and P. W. N. M. van Leeuwen, *Chem. Soc. Rev.*, 2009, **38**, 1099–1118.
105 Z. Freixa and P. W. N. M. van Leeuwen, *Dalton Trans.*, 2003, 1890–1901.
106 W. Tang, B. Qu, A. G. Capacci, S. Rodriguez, X. Wei, N. Haddad, B. Narayanan, S. Ma, N. Grinberg, N. K. Yee, D. Krishnamurthy and C. H. Senanayake, *Org. Lett.*, 2010, **12**, 176–179.
107 W. Tang, A. G. Capacci, A. White, S. Ma, S. Rodriguez, B. Qu, J. Savoie, N. D. Patel, X. Wei, N. Haddad, N. Grinberg, N. K. Yee, D. Krishnamurthy and C. H. Senanayake, *Org. Lett.*, 2010, **12**, 1104–1107.
108 S. Rodríguez, B. Qu, K. R. Fandrick, F. Buono, N. Haddad, Y. Xu, M. A. Herbage, X. Zeng, S. Ma, N. Grinberg, H. Lee, Z. S. Han, N. K. Yee and C. H. Senanayake, *Adv. Synth. Catal.*, 2014, **356**, 301–307.
109 G. Liu, X. Liu, Z. Cai, G. Jiao, G. Xu and W. Tang, *Angew. Chem., Int. Ed.*, 2013, **52**, 4235–4238.
110 P. Rojo, A. Riera and X. Verdaguer, *Coord. Chem. Rev.*, 2023, **489**, 215192.
111 K. A. Bunten, L. Chen, A. L. Fernandez and A. J. Poë, *Coord. Chem. Rev.*, 2002, **233–234**, 41–51.
112 C. A. Tolman, *Chem. Rev.*, 1977, **77**, 313–348.